OPTIMISED HIGH-PERFORMANCE CONCRETE SHELLS FOR PARABOLIC TROUGH COLLECTORS

Christoph KÄMPER[1a], Patrick FORMAN[1b], Tobias STALLMANN[2a], Mark Alexander AHRENS[1b], Peter MARK[1c] and Jürgen SCHNELL[2b]

[1a]M. Sc., [1b]Dr.-Ing., [1c]Prof. Dr.-Ing. habil., Institute of Concrete Structures, Ruhr-University Bochum, Universitätsstrasse 150, 44780 Bochum, Germany, christoph.kaemper@ruhr-uni-bochum.de, patrick.forman@ruhr-uni-bochum.de, peter.mark@ruhr-uni-bochum.de

[2a]Dipl.-Ing., [2b]Prof. Dr.-Ing., Institute of Concrete Structures and Structural Engineering, Technical University Kaiserslautern, Paul-Ehrlich-Strasse, 67663 Kaiserslautern, Germany, tobias.stallmann@bauing.uni-kl.de, juergen.schnell@bauing.uni-kl.de

ABSTRACT

The conceptual design of parabolic troughs made from high-performance concrete and having large aperture widths up to 10 m is presented. Thin shell structures are developed, which merge the supporting structure with the reflecting surface directly. Specific actions due to dead load and wind pressure, as well as representative pitch angles from sun tracking, are considered in a multi-level form-finding process. The challenge is to provide sufficient structural stiffness along with highly-accurate large apertures granting high optical efficiencies by multi-objective optimisation. Two potential alternatives are developed to lighten solid shells: tapered cross-sections with additional bracings and void formers of various geometrical shapes. Computational approaches to idealise and simulate such shells as composites consisting of concrete panels, plates and beams are derived and analysed. Finally, all designs are proven with respect to practical feasibility, optical accuracy and efficiency by numerical simulation.

Keywords: parabolic trough collector, high-performance concrete, multi-objective optimisation, form follows force, void formers, optical efficiency

1. INTRODUCTION

Currently, global electrical energy is generated by exploiting fossil resources such as oil, coal and natural gas, as well as by making use of nuclear potential. However, due to globally increasing energy demands, the need for renewable sources is essential and the related global contingent is growing. In the case of solar-thermal power plants, which concentrate solar radiation, parabolic trough collectors are the most mature and economic technology available today. The technique employed means that thermal energy can be harvested more effectively than it can with photovoltaics or wind turbines. At present, the largest power plants in Europe are Spanish sites named Andasol 1-3, which have a maximum performance of up to 150 MW and have a collector area of about 1.5 million square metres, enough to provide energy for approximately 200,000 residents. Additional plants are currently under construction in regions including North Africa, the Middle East and the US. Their solar fields usually consist of several rows of 150-metre-long collector modules. The most common collector type is the "EuroTrough" module with a length of 12 metres and an aperture width of about 5.80 metres. More recent developments aim to reduce costs and achieve economies of scale by increasing both the aperture width (to 7.50 metres) and the length (to 24 metres) as in the case of the "Ultimate Trough" [1, 2]. Parabolic trough collector modules are originally made from spatial steel frameworks which point-wise support curved mirror elements. The high accuracy of the attachment and stiffness of the mirror elements is claimed to focus solar radiation precisely on absorber tubes, in which oil or other fluids are heated to approximately 400°C.

However, significant further cost savings can only be expected if cheaper construction materials replace the general structural concepts. One promising design strategy is to merge supporting structure and reflecting surface directly. In this context, precast concrete elements serially produced with high-precision and in large quantities have already proven to be an economic and effective manufacturing concept elsewhere, such as in mechanised tunnelling [3 - 6]. The first known concrete solar collector has already been presented by the Swiss company "Airlight", and has been assembled from precast concrete elements carrying a proprietary multi-arc pneumatic mirror system [7]. In contrast, our approach aims to combine the structural benefits of a solid but light-weight and high-performance concrete shell with a highly precise inner surface, which also serves as a substrate for a concentrating mirror. In cooperation with the Ruhr-University Bochum and the Technical University of Kaiserslautern, a small-scale prototype made of high performance concrete has been developed that merges support and reflection in a shell-like structure (Fig. 1). Here, the reflecting surface consists of a foil that is glued flat onto the concrete surface. This small-scale prototype has an aperture that measures 2.205 x 3.20 m along it and is 2-3 cm thick. Although it lacks in size when compared to others competitive on the market, it shows the general feasibility of highly accurate concrete collectors.

2. STRUCTURAL CHARACTERISTICS AND MATERIAL RESTRICTIONS

In general, the design of concrete shells for parabolic trough collectors is subjected to structural and material restrictions. Firstly, high demand for low deformations must be fulfilled to satisfy sufficient optical performance [8]. Thereby, geometrical deviations in terms of curvature differences from a perfect parabola need to be determined and minimised. Low deformations require the structure to have sufficient bending ability and torsional stiffness. In the case of extremely thin-walled shells, additional stiffeners in well-aligned patterns along the longitudinal axis are applied to increase the structural stiffness without adding much weight. The layout of the pattern is adapted to comply with both structural and manufacturing aspects. For large apertures, sufficient structural and torsional stiffness can be

obtained by hollow cross-sections, while transversal stiffness is ensured by bulkheads of specific distances. Additionally, an innovative rocker bearing has been developed to keep the cross-section's centre of gravity on a horizontal axis so that no mechanical work is needed during sun tracking. These modifications offer new opportunities in the design of modules in terms of dimensions and the structural system itself. According to the material, cracking of the concrete shell must be avoided to ensure low deformations. A linear-elastic material behaviour up to the concrete's tensile strength f_{ct} is assumed and gives the stress-strain relationship according to Eq. (1):

$$\sigma_c = E_c \, \varepsilon_c \quad \text{for} \quad 0 \leq \sigma_c \leq f_{ct} \quad (1)$$

The high-performance concrete used to manufacture the prototype is based on Nanodur® cement, which is characterised by fine aggregates ($\leq$ 3 mm). With respect to the expected loads, its compressive strength is only of minor interest. It is rather the flexural strength that limits the shell's design by means of allowable principal stresses. Moreover, Young's modulus is relevant since it determines a material's stiffness and thus highly influences computational deformations. The relevant material characteristics of the high-strength concrete are summarised in Table 1.

Figure 1: *Prototype of the thin-walled concrete shell*

Table 1: Material properties of Nanodur® concrete (mean values)

Description	Value
Young's modulus E_c	47600 N/mm²
Flexural strength $f_{ctm,fl}$	15 N/mm²
Compressive strength f_c	109 N/mm²
Density ρ_c	2524 kg/m³

Besides, steel fibres embedded into the concrete increase its tensile bearing capacity [9]. However, embedded fibres are only activated if the concrete cracks. Then they bridge cracks and transfer forces. While the post-cracking behaviour is surely improved since it is more ductile now, the bending stiffness still decreases significantly compared to non-cracked concrete.

3. ACTIONS ON PARABOLIC SHELLS

3.1. General

Parabolic troughs are subjected to combined loads. Besides dead loads, which are mainly material and size dependent, the most important stresses and deformations on a single collector are induced by the module's rotation when tracking the sun and actions of the wind. In general, two situations must be distinguished with respect to wind intensity:

- Service conditions under moderate wind loads while tracking the sun. Low deformations occur and therefore maximum power is generated. It is crucial to avoid any cracking of the shell.

- Storm situation. The collector rests in safety position, in which only the structural integrity of the shell must be ensured.

In this context, it is well-established to assume a reference wind speed of 10 m/s in service conditions, whereas wind speeds of up to 35 m/s might arise in storm situations.

Furthermore, one has to distinguish between different actions that induce stresses and deformations, as well as others that alter deformations. While dead and wind load induced deformations and stresses dominate the structural design and determine its bearing capacity, initial deformations, temperature constraints, and long-term material properties of concrete alter its state of deformation and thus only influence the accuracy of

the shell's surface and expected energy gains. However, deformations are to be considered for duly assessing optical performance.

Approaches that comprise time and material dependent deformation models to capture creep and shrinkage, as well as temperature constraints and suited initial deformations due to unintended manufacturing defects, have been published in [10, 11] and adopted here. Therein, temperature constraints have been derived for a potential reference location and split into constant differences ($\Delta T_N = \pm 30$ K) and linear gradients ($\Delta T_M = 5$ K), and are weighted to account for correlation in common appearance. Besides direct actions on the parabolic shell, subsidiary parts of the substructure, like pylons or fundaments, are also affected by actions. These actions, as well as torsion potentially caused by a common driving system of jointly assembled collectors, should be generally accounted for. However, this is beyond the scope of this paper.

3.2. Dead Load

Vertical deformation of the parabolic trough shell arises mainly from dead load regarding the high-performance concrete's density (cf. Table 1). The bigger the shell, the bigger its surface; in line with potential energy gains. However, the bigger the shell, the heavier it is, and the higher deformations induced by dead load are. Moreover, the heavier the shell is, the higher its stiffness must be, in order to comply with the accuracy needs of reflection. Finally, if the shell's centre of gravity does not entirely coincide with the rotation axis, torsion will be induced by dead load, too. Small deviations are inevitable due to construction accuracy, and so the shell must provide sufficient torsional stiffness to transfer torsion to the supports.
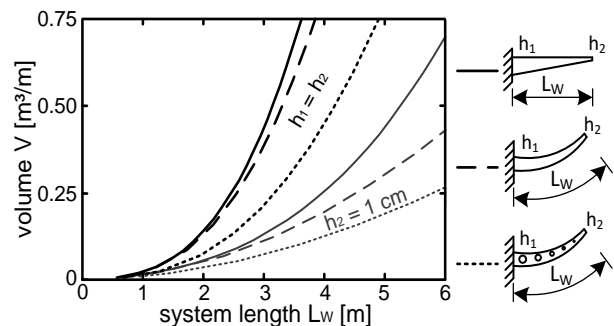

Figure 2: Concrete demand by means of the system length of a cantilever beam

Thus, the shell's design is a multi-objective optimisation task, aiming for minimised self-weight along with maximum bending and torsional stiffness. Mutual dependencies are studied in the following examples.

The concrete volume, and thus its weight, increases exponentially with the aperture width, as shown in Figure 2. This is analysed by transferring the parabolic shell into an equivalent cantilever beam with a rectangular cross-section and assuming its length L_W equal to half the curved aperture width of a trough. The shape of the cantilever is also varied. Altogether, three cases are analysed. At first, the height of a purely horizontal cantilever varies linearly from h_1 at clamping to h_2 at the free end. Thereby, the latter is restricted to at least 1 cm. The shape is then altered to be parabolic, and finally, additional void formers are introduced to save some weight. All structures are subjected to dead load and an additional orthogonal wind load on the upper surface, while restricting the maximum elastic stresses at clamping to 5 N/mm².

An exponential relationship between demand for concrete and the cantilever's length exists for all cases. The greater the length shall be, the more material is generally needed. However, compared to constant heights, the amount of concrete is greatly decreased for tapered systems, in line with a flatter curve of this case. This is even truer when compared with parabolic shaped systems, especially in the case of hollow sections.

An alternative to designs with full or hollow cross-sections is bracings as strengthening ribs, such as common T-profiles. Thereby, T-profiles hold great potential to reduce self-weight with respect to an equivalently stiff full cross-section. In this regard, Figure 3 compares the required amounts of concrete of equivalent cantilever beams with different cross-sections by means of the aperture width. Again, three cases are analysed: a tapered system with $h_2 = 1$ cm, a solid cross-section and a hollow one (detailed in Figure 2). These are now supplemented by one that is T-shaped. While the input remains unchanged from the previous example, the corresponding deformations are also computed. Apparently, for small apertures as in the case of the prototype, slender shells with solid sections are preferable, since material savings by alternative but more complex shapes are minor and manufacturing can get complicated. For troughs with an aperture

width of less than 6.00 m, such as the "EuroTrough" collector, a design with bracings seems to be appropriate. In this case, the maximum concrete savings are achieved and the deformations are still sufficient. The deformations are about 5 cm, which would be too large for a parabolic trough system. However, here they only represent the stiffness for an equivalent system; the true bearing behaviour of shells would significantly lower the deformations.

Hollow cross-sections are recommended for large aperture collectors (LAC). The concrete savings balance additional manufacturing efforts. Moreover, the stiffness stays on a similar level compared to the solid case. In contrast, a system with bracings would be inappropriate because of the high deformations.
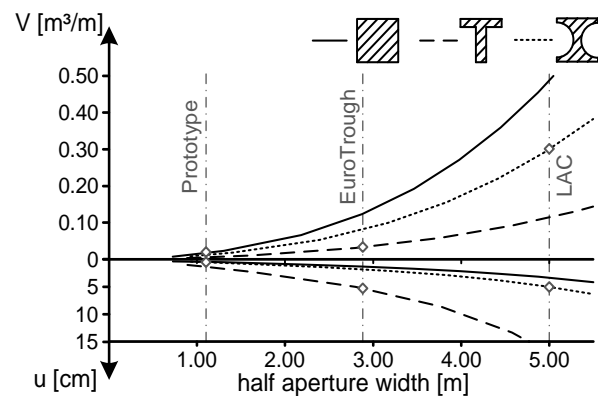

Figure 3: Concrete demand and deformations by means of the aperture width for an equivalent cantilever system and different cross-sections

These first analyses lead to three potential design concepts that all differ with respect to the demand of concrete and the expected manufacturing costs. These are:

- single-walled shells: mass ↑, costs ↓

- shells with bracings: mass ↓, costs →

- hollow structures: mass ↘, costs ↑

3.3. Wind Loads

In addition to dead loads, wind loads also strongly influence structural deformations. However, they are not constant but highly dependent on the interaction between the structure and the wind flow. When tracking the sun, multiple load cases appear.

To capture the special wind loads on collector shells, wind tunnel tests have been performed on a single parabolic trough model in the boundary layer wind tunnel at the Ruhr-University Bochum [10, 11, 12]. The measured pressure differences over time on the surface of the model result from a statistical analysis of the extreme values, according to Cook [13]. It delivers equivalent wind load coefficients $c_{p,net}$, which are valid for a return period of 50 years and variable over the aperture width of the parabolic shell. To determine the local wind loads q_w on the parabolic surface, the equivalent coefficients must be multiplied by the gust pressure q_{ref} for a reference height of $z = 10$ m.

$$q_w = c_{p,net}\, q_{ref} \qquad (2)$$

Another method is to determine the global, external forces and moments onto the collector as non-dimensional coefficients. The lines of application of the forces are depicted in Figure 4.
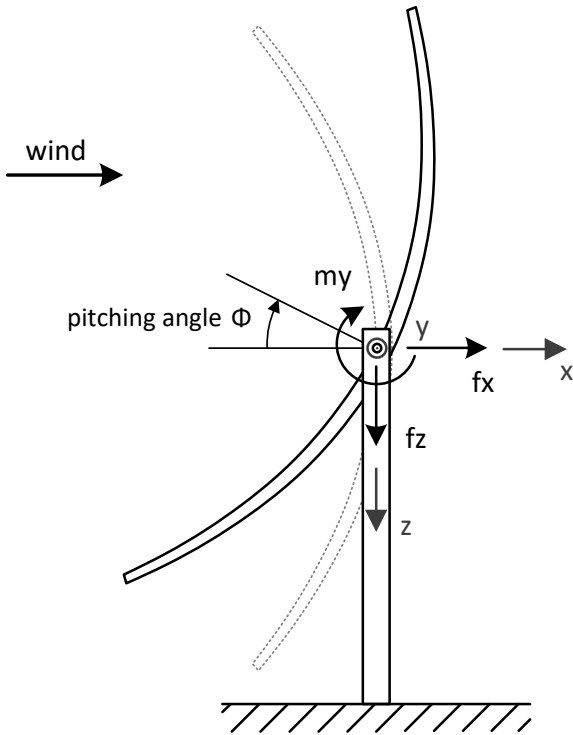

Figure 4: *Definition of the coordinate system and forces*

Based on the variable pressure distribution over the aperture width, the global aerodynamic loads (f_x, f_z, m_y) have been derived. They are defined by means of non-dimensional coefficients as follows:

horizontal line force f_x $\quad C_{fx} = f_x/(q_{ref}\, w\, l)$ $\qquad (3)$

vertical line force f_z $\quad C_{fz} = f_z/(q_{ref}\, w\, l)$ $\qquad (4)$

pitching moment m_y (per m) $\quad C_{my} = m_y/(q_{ref}\, w^2\, l)$ $\quad (5)$

Thereby, w is the aperture width and l is the length of the collector module. Since the pressure distribution has only been derived for one axis at the centre, the length is set to 1 m/m. Well-reasoned by the correlation length of the wind profile, one could also use the total collector's length to determine the global loads. The evaluation of the global coefficients is performed for four different pitching angles Φ. Thereby, the mean (m), minimum (min) and maximum (max) values are calculated (Table 2). These values can be used to gain the global loads onto the parabolic shell modules.

Table 2: *Global, non-dimensional coefficients for different pitching angles*

Φ [°]	C_{fx} max	min	m	C_{fz} max	min	m	C_{my} max	min	m
0	3,04	0,41	1,29	0,06	0,00	0,01	0,00	-0,04	-0,01
45	2,78	0,35	1,13	3,35	0,36	1,27	-0,01	-0,29	-0,08
90	0,25	0,18	0,13	1,18	-1,02	-0,15	0,17	0,13	0,09
135	1,50	0,10	0,63	0,19	-0,82	-0,30	0,34	0,15	0,17

4. EVALUATION OF THE SURFACE ACCURACY AND OPTICAL EFFICIENCY

The primary aim of parabolic trough collectors is to focus direct solar irradiation on line-like absorber tubes. For this reason, the reflecting surface has to be as accurate as possible. This means it must be almost free from deformation and therefore have an ideal parabolic shape in its cross plane. Deformations in longitudinal direction are relatively unimportant, hence the offset of solar rays will only take place along the focal line. However, deformations of the parabolic surface, such as those due to dead and wind load, lead to slope deviations of the reflecting surface that cause slope errors of the reflected solar rays. Depending on the distance, caused by the slope error, between the reflected

solar rays and the focal point, and the diameter of the absorber tube, the optical efficiency can be determined based on a distorted surface.

Therefore, an angular acceptance function f_{PT} has been derived in [14] which weights the distance of the solar rays to the focal point as a function of the slope error. The geometric situation is shown in Figure 5. The acceptance function is restricted by the so-called acceptance half angle θ_1, which defines the maximum angle of reflection for a solar ray at the parabolic edge. This means that for every slope error θ_x caused by a distorted surface less than θ_1, the reflected solar ray will be focused onto the absorber tube. The geometric pendant of θ_1 for the apex of the parabola is defined as the second acceptance half angle θ_2. For every slope error greater then θ_2, the reflected ray will miss the absorber. Between the half angles, the efficiency will be interpolated according to Eq. (6).

$$f_{pt}(\theta)=\begin{cases} 1 & \text{for } |\theta|<\theta_1 \\ cot\frac{\varphi_r}{2}\left(\frac{2\ tan\frac{\varphi_r}{2}}{C\ \theta}-1\right)^{\frac{1}{2}} & \text{for } \theta_1<|\theta|<\theta_2 \\ 0 & \text{for } |\theta|>\theta_2 \end{cases} \quad (6)$$

with

$$\theta_1=\frac{sin\ \varphi_r}{C} \quad (7)$$

$$\theta_2=\frac{2\ tan\frac{\varphi_r}{2}}{C} \quad (8)$$

$$C=\frac{w}{d} \quad (9)$$

Thus, it is recommended to restrict the slope error as much as possible in the design of efficient troughs made from high-performance concrete, to the acceptance half-angle θ_1. Thereby, the parameter C in Eq. 9 represents the concentration ratio – in this case the geometric concentration ratio – which defines the rate of reflected to absorbed solar radiation. It is an essential value for the operating temperature of the heat transfer fluid.

The opening angle φ_r describes the angle between the parabola's apex and the edge of the segment.

Since the dimensions of the parabolic trough and the corresponding absorber tube diameters differ from trough to trough, the acceptance function varies for every specific collector.
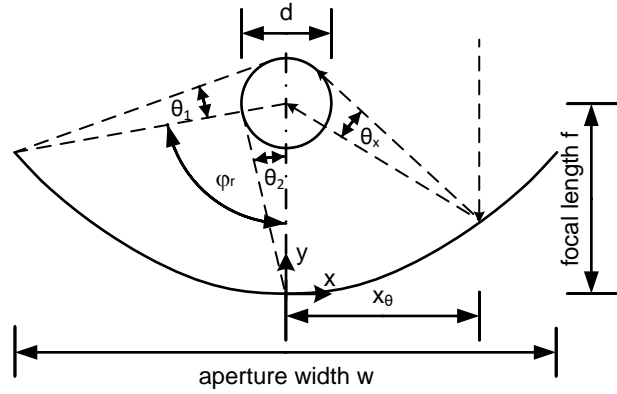

Figure 5: Geometry to derive the acceptance function, adapted from [14]

However, for the determination of the global efficiency η, the local efficiency distribution over the collector's surface, defined by the acceptance function, has to be integrated. Additionally, the distribution of the overall slope errors is fully defined by its two basic characteristics, mean value μ and standard deviation σ. These two values serve as references for further investigation. As an example, Figure 6 shows the frequency distribution of the prototype's slope error, which is overlaid with the acceptance function. The distribution is weighted with the acceptance function shown in red. As long as the slope error distribution lies between the dashed lines, which mark the acceptance half angle θ_1, full efficiency is reached.
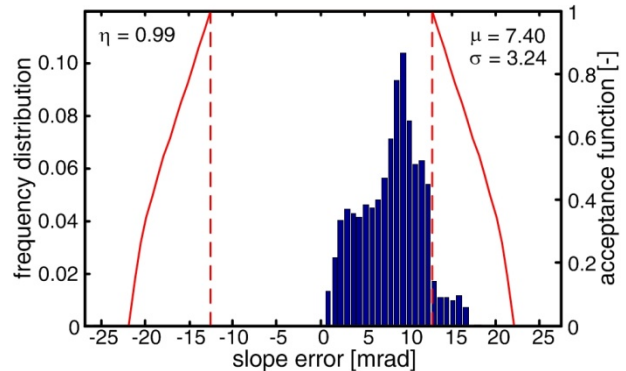

Figure 6: Slope error based accuracy evaluation

5. CONCEPTUAL DESIGNS

5.1. Collector modules with global bracing strategy

Successful realisation of the concrete prototype proves the potential of slender shells as parabolic

trough elements. However, the dimensions of the prototype with an approximately 2.20 m aperture width, do not suffice for power plants, since the amount of concentrated solar radiation is too low for an economic operating temperature. To improve efficiency, the aperture width must be increased. The module should be enlarged to at least the dimensions of the commercially well-established steel collector module "EuroTrough", which has an aperture width of 5.77 m and a module length of 12 m. As shown above, a solid shell will not be appropriate, and therefore additional bracings are needed. These bracings should at best follow the flux of forces and should be attached to the outer surfaces so that no shading of the reflecting surface is created. An optimal arrangement of bracings is identified by means of topology optimisation [15, 16].

The objective of topology optimisation is to minimise the compliance c of a discretised structure, and equivalently to maximise its stiffness. Thereby, the material distribution as a function of the so-called pseudo-density ρ is iteratively changed until the objective function converges. Please note that the optimised structure uses a reduced design space Ω only, which is defined by the reduction

factor ω. The optimisation problem can be written in matrix notation as follows:

$$\min c(\rho_i) = \min \mathbf{u}^T \mathbf{K}\, \mathbf{u} = \min \sum_{i=1}^{n} E_i(\rho_i)\mathbf{u}_i^T \mathbf{K}_{i,0}\mathbf{u}_i \quad (10)$$

considering the restrictions:

$$\Omega(\rho)\,/\,\Omega_0 = \omega \qquad (11)$$

$$0 < \rho \leq 1 \qquad (12)$$

with: **K**: stiffness matrix

u: displacement vector

The Young's modulus E of each element i is determined regarding the optimisation variable ρ_i.

$$E_i(\rho_i) = E_{min} + \rho_i^{\eta}(E_0 - E_{min}) \qquad (13)$$

Thereby, E_0 is the initial Young's modulus of the material, E_{min} a numerical value to avoid singularity and η a penalty factor according to the SIMP (Solid Isotropic Material with Penalisation) algorithm [17], which serves to achieve faster convergence and should prevent from graded areas as well.
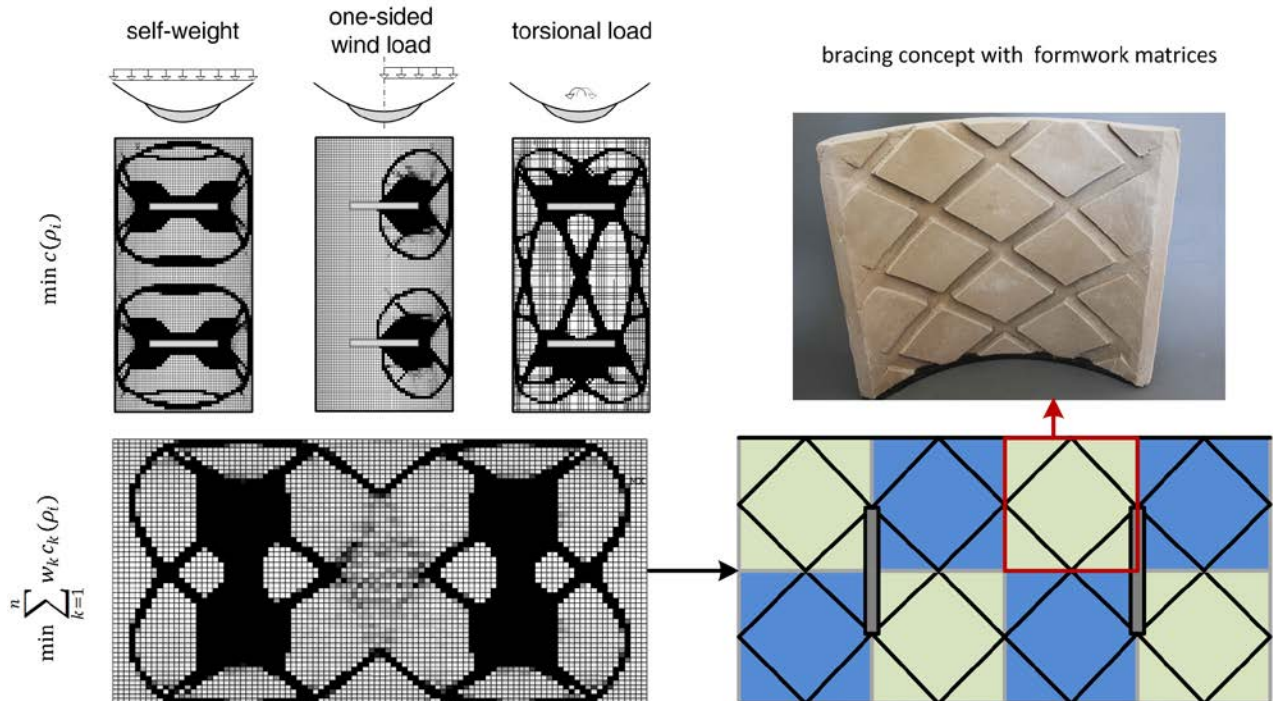

Figure 7: *Topology optimisation results: distribution of the pseudo density ρ_i (black = 1, white ≈ 0) (left), identified bracing concept with 4x2 identical matrices and a formwork made of sand with bracings (right)*

Exemplarily on a model with rocker bearings and an aperture width like the "EuroTrough" module, topology optimisation has been performed three times, considering the main load effects which here have been simplified as constant loads (Figure 7, left). Each optimal design obtained is thus only able to bear its special load situation. Each optimisation result divides the design space into black and white elements. Black elements mark positions where material and stiffness are required while white ones are dispensable.

To consider multiple load cases, a multi-objective optimisation problem must be solved. Therefore, the sum of compliances of all load cases is minimised, whereby the individual compliances are weighted by means of factors w_k. Thus, the initial optimisation problem according to Eq. (10) is modified to:

$$\min \sum_{k=1}^{n} w_k c_k(\rho_i) \qquad (14)$$

In the case of equally weighted compliances ($w_1 = w_2 = w_3$), the optimal result from Eq. 14 is shown at the centre of Figure 7. Although some areas in the middle of the shell are unintentionally graduated, a bracing concept with a diamond shaped pattern and additional edge bracings is clearly identifiable.

This pattern can be adopted and divided into 4 x 2 identical matrices. For these, a formwork made from high-performance concrete can be built up, which consists of two identical segments. These are to be constructed four times, employing freely re-shapeable frozen sand negative formworks that deliver highly accurate surfaces in a hardened state (Figure 7, right). Overall, this small-scale example of topology optimisation based design and identification of bracings proves to be of practical use more generally.

5.2. Large aperture collectors (LAC)

Following current trends of up-scaling conventional collectors to increase the geometrical concentration ratio C, the aim is a parabolic trough made of high-performance concrete with an aperture width of 10 m. To realise such dimensions with concrete,

sufficient structural stiffness in transversal direction must be ensured to guarantee a high optical performance. Therefore, the outer surfaces of the concrete module must be fitted first, which leads to a tapered course of wall-thickness from the vertex to the edges, as shown above. This ensures that the internal lever arm of forces increases and delivers adequate structural stiffness.
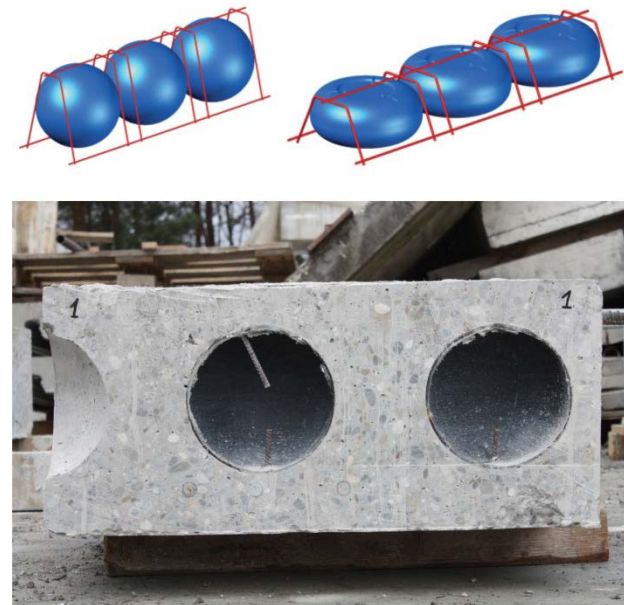

Figure 8: *Types of void formers; Eco-Line (sphere) and Slim-Line (flat void former) by cobiax®-technology (Top, Source: www.cobiax.com) and a hollow core slab section with spherical void formers (Bottom: Source: TU Kaiserslautern)*

Next, and most efficiently, the homogeneous cross-section can be dissolved into an inhomogeneous one employing void formers. Void formers have already proven successful when applied in arbitrary concrete slabs [18]. Here, rotationally symmetric and spherical shapes or flattened ellipsoids are often used. They are arranged in retaining rebar cages and embedded into concrete between the top and bottom reinforcement layers during construction (Figure 8).

Fabricated that way, hollow core slabs of equivalent length allow for significant volume reductions along with tolerable losses of (bending) stiffness, in contrast to solid cross-sections. They also still comply with common limits of serviceability (SLS) and thus enable larger spans [19].
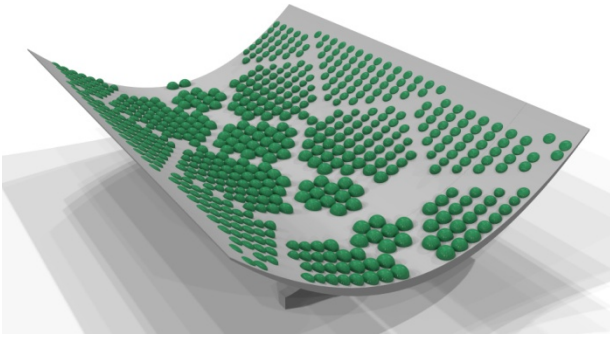
112

Figure 9: *Concept of a large aperture parabolic trough collector with spherical void formers and global bracings*

The strategy used to apply void formers can be transferred to large aperture collector (LAC) modules by adapting retaining cages and void formers with different sizes according to the geometry of the cross-section (Figure 9). Between the void formers, solid regions remain in longitudinal and transversal directions that can be sheltered by templates during construction [19, 20]. Inspired by Figure 7, the distribution of void formers in a concrete matrix can thus be guided by topology optimisation. It delivers solid zones where global stiffeners or bracings should be provided, while intermediate parts are to be filled with void formers. Additionally, vector fields of principal stresses obtained from finite element analyses can be adapted to distribute void formers according to the bearing behaviour [21].

5.3. Volume reduction and effective stiffness values for large aperture collectors
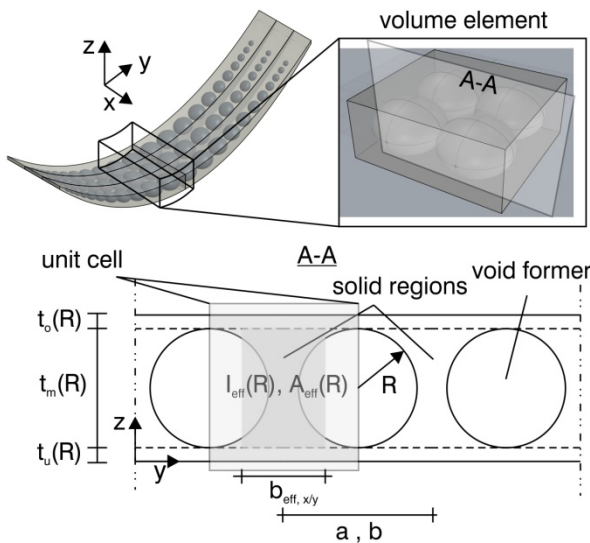

Figure 10: *Volume element with periodical ordered void formers and a representative unit cell*

For a numerical analysis of large aperture collector modules with different void formers, effective stiffness values and the corresponding volume reduction must be determined in advance to predict deformations. Therefore, a simplified approach is introduced which is based on a volume element that is cut from a collector module containing regularly arranged void formers (Figure 10).

This volume element can further be reduced to a representative unit cell of the outer dimensions *a, b* and *h* whose elastic properties can be determined in the remainder and assigned to the entire structure. However, it should be noted that this way neglects the geometrical curvature of the shell.

Although the unit cell is originally 3D, an engineering approximation that helps to determine the cell's elastic properties is appropriate. Thus, the cell is set-up as a multilayer composite made from multiple, but 2D, layers with stiffness properties of slabs, panels and beams. Thereby, deformations due to shear are neglected (Kirchhoff-Love theory). The top and bottom layers of the cell, with thicknesses of t_o and t_u, respectively, are defined as homogeneous, isotropic cover layers. The solid region in between, also limited by two consecutive void formers, is idealised with respect to the void's radius R as longitudinal, and transversal stiffeners with a stiffness spread over the distances a and b (Figure 11). The stiffness of the multilayer composite follows from the total sum of all single layers, including all individual axial and bending stiffness components. Of course, the orthogonal orientation of stiffeners leads to an orthotropic elastic behaviour.
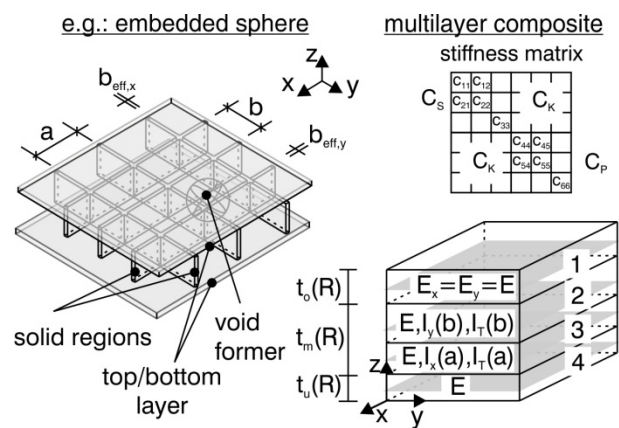

Figure 11: *Symmetrical orthotropic surface element as a multilayer composite*

113

In matrix notation, internal stresses $\mathbf{n}_i$ and strains $\boldsymbol{\varepsilon}_i$ of a single layer i are coupled by the elastic stiffness matrix $\mathbf{C}_i$ according to Eq. (15):

$$\mathbf{n}_i = \mathbf{C}_i \boldsymbol{\varepsilon}_i \qquad (15)$$

or employing components according to Eq. (16):

$$\begin{bmatrix} n_x \\ n_y \\ n_{xy} \\ m_x \\ m_y \\ m_{xy} \end{bmatrix} = \begin{bmatrix} c_{11} & c_{12} & c_{13} & & & \\ & c_{22} & c_{23} & & \mathbf{C}_K & \\ \text{sym.} & & c_{33} & & & \\ & & & c_{44} & c_{45} & c_{46} \\ & \mathbf{C}_K & & & c_{55} & c_{56} \\ & & & \text{sym.} & & c_{66} \end{bmatrix} \begin{bmatrix} \varepsilon_x \\ \varepsilon_y \\ \gamma_{xy} \\ \kappa_x \\ \kappa_y \\ \kappa_{xy} \end{bmatrix} \qquad (16)$$

Observing the orthotropic properties, components c_{13}, c_{23}, and c_{46}, c_{56} of the stiffness matrix vanish so that symmetrical stresses (n_x, n_y) do not affect anti-symmetrical strains (γ_{xy}) anymore and bending (κ_x, κ_y) and twisting (κ_{xy}) are uncoupled [22]. Assuming the multilayer composite subjected to bending and in plane axial stresses ($z = 0$), the distortion of an arbitrary layer's middle surface is obtained from Eq. (17),

$$\varepsilon_i = \varepsilon_0 + z_i \kappa \qquad \kappa = \kappa_i \qquad (17)$$

in which the equilibrium of internal stresses according to $z = 0$ employs:

$$n_0 = \sum n_i \qquad (18)$$

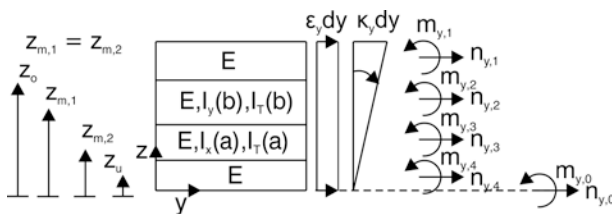$$m_0 = \sum m_i + z_i n_i \qquad (19)$$

Figure 12: *Stresses and strains related to a general composite subjected to bending and axial stresses*

By contrast, if the composite is non-symmetric, the general relations according to Figure 12 with respect to an arbitrarily chosen reference level z are obtained as shown in Eq. (20) and (21).

$$\mathbf{n} = \mathbf{C}_S \boldsymbol{\varepsilon} + \mathbf{C}_K \boldsymbol{\kappa} \qquad (20)$$

$$\mathbf{m} = \mathbf{C}_K \boldsymbol{\varepsilon} + \mathbf{C}_P \boldsymbol{\kappa} \qquad (21)$$

The composite axial ($\mathbf{C}_S$), bending ($\mathbf{C}_P$) and coupled ($\mathbf{C}_K$) stiffness matrices result from the sum of the single layers' stiffness contributions

$$\mathbf{C}_S = \sum \mathbf{C}_{Si} \qquad (22)$$

$$\mathbf{C}_K = \sum z_i \mathbf{C}_{Si} \qquad (23)$$

$$\mathbf{C}_P = \sum \mathbf{C}_{Pi} + z_i^2 \mathbf{C}_{Si} \qquad (24)$$

regarding individual distances z_i of the layers' mid-planes with respect to the reference plane ($z = 0$). Assuming a centric multilayer composite ($\mathbf{C}_k = 0$) and neglecting axial stresses ($n = 0$), the bending stiffness matrix of the composite simplifies to

$$m = (\mathbf{C}_P - \mathbf{C}_K \mathbf{C}_S^{-1} \mathbf{C}_K)\kappa \qquad m = \mathbf{B}\kappa \qquad (25)$$

with $\mathbf{B} = \mathbf{C}_p$. The single components of the stiffness matrix $\mathbf{C}_p$ follow from Eq. (26) - (28) for the cover layers (index C) and the orthogonal stiffeners (index St) regarding the second moments of area in case of bending (I) and torsion (J).

panel:

$$c_{11,C} = \frac{E_x t}{1 - v_x v_y} \qquad c_{22,C} = \frac{E_y t}{1 - v_x v_y} \qquad c_{33,C} = G_{xy} t$$

$$c_{12,C} = \frac{E_y v_x}{1 - v_x v_y} \qquad c_{21,C} = \frac{E_x v_y}{1 - v_x v_y} \qquad (26)$$

slab:

$$b_{44,C} = \frac{E_x t^3}{12(1 - v_x v_y)} \qquad b_{55,C} = \frac{E_y t^3}{12(1 - v_x v_y)} \qquad b_{66,C} = \frac{G_{xy} t^3}{12}$$

$$b_{45,C} = \frac{E_y t^3 v_x}{12(1 - v_x v_y)} \qquad b_{54,C} = \frac{E_x t^3 v_y}{12(1 - v_x v_y)} \qquad (27)$$

beam:

$$c_{11,St} = \frac{EA_x}{b} \qquad b_{44,St} = \frac{EI_y}{b} \qquad b_{66,St} = \frac{GJ_x}{4b} \qquad (28)$$

Figure 13 compares normalised effective stiffness and volumes of a unit cell with void formers of spherical and cylindrical shape. Normalised bending and torsional stiffness follow from Eq. (29) and (30), respectively,

$$b_v = \frac{Et^3}{12(1-v^2)} \qquad (29)$$

$$c_v = \frac{Et}{1-v^2} \qquad (30)$$

while the reference volume is simply obtained by multiplication regarding a unit cell without voids.

First, the relative stiffness reduction of unit cells with cylindrical voids is always greater than with spherical ones. Second, in comparison, the effective axial stiffness decreases faster than the bending stiffness. Third, up to a ratio of 40%, the voids do not have any significant influence on the stiffness in longitudinal direction. Only in transversal direction does the unit cell with an embedded cylinder lose significant stiffness. With larger d/h ratios, the curve of the bending stiffness even crosses the one, indicating a relative volume decline ($d/h \approx 0.8$). This is reasoned by a then considerably reduced stiffness of the cover layers. The unit cell's stiffness merely remains, due to a few centimetre-thick stiffeners and moments of inertia.
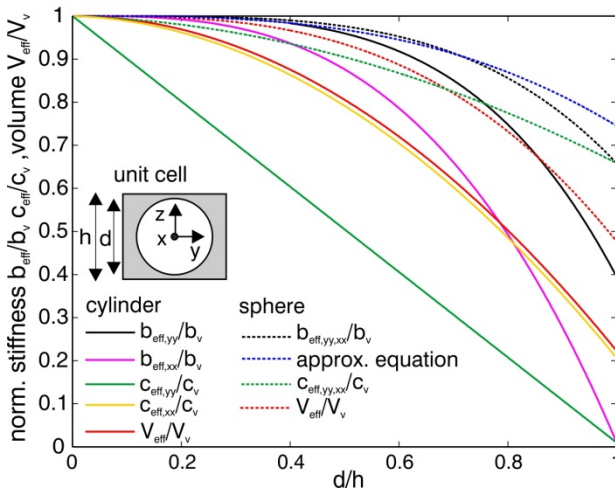

Figure 13: *Normalised effective values for bending and axial stiffness ($b_{eff,xx,yy}$, $c_{eff,xx,yy}$) as well as volume of a single cell with various void formers*

By contrast, the relative stiffness reduction of a unit cell with spherical voids is always lower than the relative volume decline. In this case, the elastic deformations that occur are lower than in a solid cross-section. Comparison to an approximated bending stiffness for cross-sections with voids, published in [23], confirms the calculated stiffness up to $d/h = 0.8$. With higher ratios, the stiffness according to the unit cell concept provides conservative results. Hence, the unit cell approach for determining effective stiffness can be recommended for other shapes of voids.

In general, cylindrical voids deliver a greater volume reduction than spherical voids do. However, this also comes with greater bending and axial stiffness losses with higher d/h-ratios and increased deformation, especially in transversal direction, that must carefully be taken into account when analysing optical performances.

6. NUMERICAL MODELLING AND OPTICAL PERFORMANCE

6.1. Collector module with global bracings

A collector module with bracings (detailed in Sec. 5.1) with an aperture width of 5.77 m, like the "EuroTrough" collector, has been discretised and analysed by finite elements (Figure 14, top). Since the model employs parameters to regulate its geometry, the shell is form optimised at first, as is generally recommended in hierarchical optimisation. The primary optimisation variables are the width and height of the bracings, having a constant, rectangular cross-section. The minimisation of the mass is the objective function, while principle stresses in the bracings and surface deformations are restricted. Optimisation results in outer bracings having a width of 5 cm and a height of 18 cm.

For a verification of the accuracy and therefore the optical efficiency, the deformations of the collector surface have been computed for a fixed pitch angle of 45°, for which the maximum wind loads occur. The maximum distortion of the parabolic surface results in deformations up to 5 mm, occurring mainly at the corners of the surface (Figure 15, top). This leads to the slope errors of the reflected solar rays in Figure 15 (centre). The efficiency measure is shown in Figure 15 (bottom). Due to the fact that the slope error lies between the dashed lines, a full

optical efficiency of the whole collector module ($\eta = 1$) is reached. With respect to the statistical values $\mu = 0.19$ mrad and $\sigma = 2.34$ mrad, only small deflections of solar rays being reflected must be expected. Initial but unintended effects from torsion due to assembling of modules to collectors is therefore something that can be largely compensated for.
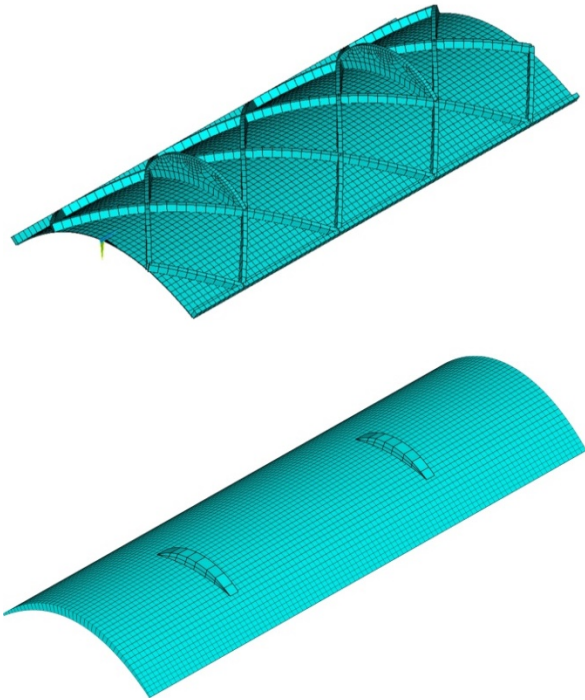

Figure 14: *Finite-element models of parabolic shells with bracings (top) and a tapered cross-section in case of the LAC (bottom)*
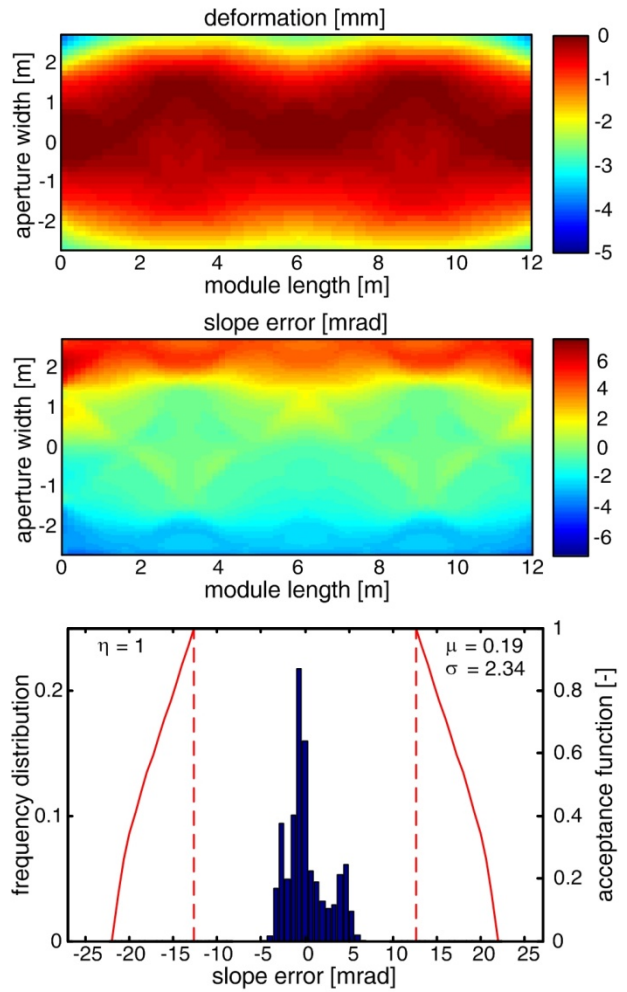

Figure 15: *Surface deformations (top) and corresponding slope errors (centre) along with accuracies (bottom)*
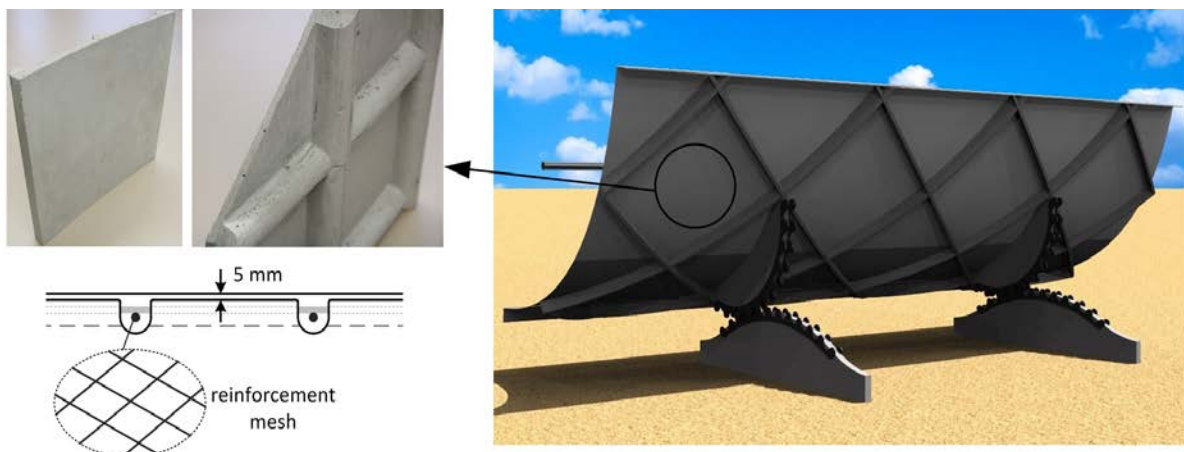

Figure 16: *3D Visualisation of a parabolic shell collector module with outer bracings and rocker bearings (right). Front and back view of a reinforced concrete sample with minimal thickness (left)*

A first visualisation of such a parabolic shell module with outer, diamond-shaped bracings in 3D is shown in Figure 16. A special feature of this model is the design of the shell. Whereas the bracings are the main bearing elements, the shell structure is as thin as possible. Due to an intended ductile load-bearing behaviour, the shell contains a reinforcement mesh with minimal concrete cover. Thus, the whole shell structure is separated into a primary diamond-shaped bracing structure that serves as a global load-bearing structure and a secondary sub-structure that serves as a reflector substrate.

A first sample of such a sub-structure with a very smooth surface to apply reflectors is shown in Figure 16 (left). It has an equivalent volume thickness of 0.86 cm and its equivalent stiffness thickness is only 1.86 cm.

6.2. Analysis of a large aperture collector (LAC)

Figure 17 shows the optical analysis of an LAC module with an aperture width of 10 m, a length of 30 m, and a height of 0.5 m at vertex evaluated for a pitch angle of 45°, adapting wind loads detailed in Sec. 3.3. A ratio of $d/h = 0.8$ for spherical void formers, with corresponding values for volume and stiffness, has been taken into account.

The finite element model consists of 4-noded shell elements with a tapered thickness from vertex to the edges (Figure 14, bottom). The length of the cantilever is 40% of the distance between the rocker bearings, providing nearly the same vertical deformations at the cantilever ends as at mid-span.

Due to high structural stiffness, especially in transversal direction, low deformations generally occur. Compared to the collector module with bracings, the slope error's distribution appears one-sided with a low standard deviation. Accordingly, a full optical efficiency is reached ($\eta = 1.0$). The low standard deviation of the error in this case gives room for further optimisation of the weight, accepting moderate stiffness losses. This indicates that a coupled multi-objective optimisation of mass and slope error seems to be an appropriate approach for gaining even more economic designs.
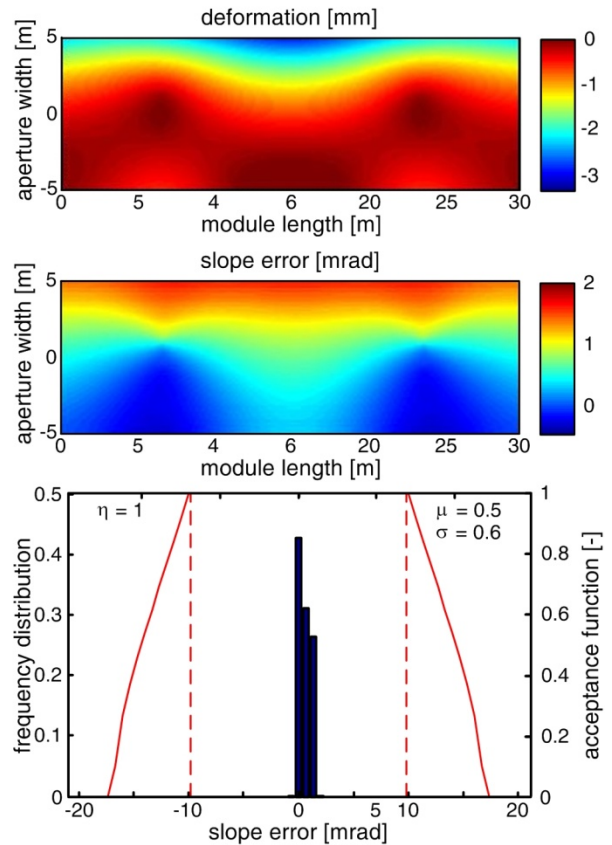

Figure 17: *Surface deformations (top) and corresponding slope errors (centre) along with accuracies (bottom) for an LAC with d/h = 0.8*

7. CONCLUSIONS

Parabolic-curved shells made of high-performance concrete have a high potential to be competitive on the market and offer an economic friendly alternative to conventional spatial steel frameworks. The concrete's great tensile strength, formed by utilising a structural shell with glued-on mirror elements, enables such light-weight collectors to possess formidable stiffness. Well-established and highly automated manufacturing procedures for precast elements in serial production, inspired from fabrication and installation of segmental linings in mechanised tunnelling, can be easily adopted. So far, for "EuroTrough" type collector modules with aperture widths of approximately 6 m, a thin solid shell with additional stiffeners turns out to be the most mature solution for cases where the shell is only a few centimetres thick. For larger apertures, another strategy needs to be considered. Necessary

material reductions with a moderate loss of stiffness can be achieved by hollow cross-sections applying void formers in the central axis. Effective stiffness properties have been computed to quantify the influence of volume reduction and stiffness losses. Two conceptual design alternatives grant sufficient optical performance and provide structural, manufacturing and process benefits when compared to conventional collectors made of spatial steel frameworks.

ACKNOWLEDGMENTS

REFERENCES

[1] **Riffelmann, K.-J., Richert, T., Nava, P., Schweitzer, A.**, Ultimate Trough® - A significant step towards cost competitive CSP; *19th SolarPACES Conference*, Las Vegas, NV, USA, September 2013.

[2] **Marcotte, P. and Manning, K.**, Development of an advanced large-aperture parabolic trough collector. *In: Proceedings of the SolarPACES International Conference*, Beijing, China, 2013, Energy Procedia, 49, S. 145–154.

[3] **Kämper, C., Putke, T., Zhao, C., Lavasan, A., Barciaga, T., Mark, P. and Schanz, T.**, Vergleichsrechnungen zu Modellierungsvarianten für Tunnel mit Tübbingauskleidung. *Bautechnik 93 (2016)*, Heft 7, Ernst & Sohn Verlag, Berlin, 2016.
[DOI: 10.1002/bate.201500064]

[4] **Putke, T.; Bohun, R. and Mark, P.**, Experimental analyses of an optimized shear load transfer in the circumferential joints of concrete segmental linings, *Structural Concrete*, Volume 16, Issue 4, pp. 572-582, 2015.
[DOI: 10.1002/suco.201500013]

[5] **Guidelines of the Working Group "Segmental Ring Design" of the German Tunneling Committee (DAUB)**, *Recommendations for the design, the production and the assembly of segmental rings,* German Geotechnical Society, Paperback on Tunnel Design 2014, Ernst & Sohn, 2014.

[6] **Putke, T., Song, F., Zhan, Y., Mark, P., Breitenbücher, R. and Meschke, G.**, Entwicklung von hybriden Stahlfaserbetontübbings: Experimentelle und numerische Analysen von der Material- bis zur Bauwerksebene, *Bauingenieur*, Band 89, November 2014, S. 447-456.

[7] **Pedretti, A.**, A 3 MW Thermal concentrated solar power pilot Plant in Morocco with the Airlight Energy Technology, *18th SolarPACES Conference*, Marrakesh, Morocco, September 2012.

[8] **Pottler, K., Ulmer, S., Lüpfert, E., Landmann, M., Röger, M. and Prahl, C.**, Ensuring performance by geometric quality control and specifications for parabolic trough solar fields, *Solar Paces 2013*, Energy Procedia, 49, 2014, pp. 2170 – 2179.

[9] **Heek, P., Ahrens, M.A., Mark, P.**, Incremental-iterative model for time-variant analysis of SFRC subjected to flexural fatigue, *Materials and Structures*, 50(1), 2016, pp. 1-15.
[DOI: 10.1617/s11527-016-0928-z]

[10] **Forman, P., Müller, S., Ahrens, M. A., et al.**, Light concrete shells for parabolic trough collectors – Conceptual design, prototype and proof accuracy. *Solar Energy* 111, 2015, pp. 364-377.

[11] **Forman, P., Kämper, C., Stallmann, T., Schnell, J., Mark, P.**, Parabolschalen aus Hochleistungsbeton als Solarkollektoren. *Beton- und Stahlbetonbau* 111(12), 2016, S. 851-861.
[DOI: 10.1002/best.201600051]

[12] **Oya, J., Kalender-Wevers, C., Winkelmann, U., and Höffer, R.**, Experimental and numerical investigation of the dust transport on the reflector panels of a parabolic trough power plant. *Proceedings of the European-African Conference on Wind Engineering EACWE 2013*, Cambridge, 2013.

[13] *Cook, N. J.*, *The designers guide to wind loading of building structures – part 2: Static structures*, London, Oxford: Butterworths 1990.

[14] *Bendt, P., Rabl, A., Gaul, H. W. and Reed, K. A.*, *Optical analysis and optimization of line focus solar collectors*, SERI/TR-34-092, Solar Energy Research Institute, Golden, Colorado, 1979.

[15] *Bendsøe, M. P. and Sigmund, O.*, *Topology Optimization – Theory, Methods and Applications*. 2. Auflage, Berlin: Springer-Verlag, 2004.

[16] *Putke, T. and Mark, P.*, Fachwerkmodellbildung mit topologischen Optimierungsverfahren, *Beton- und Stahlbetonbau* 109 (9), 2014, Ernst & Sohn Verlag, Berlin, pp. 618-627.

[17] *Rozvany, G. I. N.*, Aims, scope, methods, history and unified terminology of aims, scope, methods, history and unified terminology of computer-aided topology optimization in structural mechanics. *Structural and Multidisciplinary Optimization* 21 , 2001, S. 90–108.

[18] *Abramski, M., Albert, A., Nitsch, A. and Schnell, J.*, Bearing behaviour of biaxial hollow core slabs*, IABSE Symposium Report*, IABSE Symposium, Venice 2010, pp. 23-30, [DOI: 10.2749/222137810796025870]

[19] *Albrecht, C., Albert, A., Pfeffer, K. and Schnell, J.*, Design and construction of two-way spanning reinforced concrete slabs with flattened rotationally symmetrical void formers, *Concrete and Reinforced Concrete Construction*, Vol. 107, Issue 9, 2012, pp. 590 – 600.
[DOI: 10.1002/best.201200027]

[20] *Albrecht, C., Schnell, J. and Pfeffer, K.*, Voided flat slabs with rotationally symmetrical void formers - Manufacture, Installation and special features of the design, *In: Proceedings on 1st Annual International Conference on Architecture and Civil Engineering*, Singapore, 2013, pp. 290–295.

[21] *Adriaenssens, S., Block, P., Veenendaal, D. and Williams, C.*, *Shell Structures for Architecture – Form Finding and Optimization*, Routledge Taylor & Francis Group, 2014.

[22] *Wiedemann, J.*, *Leichtbau – Elemente und Konstruktion*, 3. Auflage, Springer-Verlag, 2007.

[23] *Schnellenbach-Held, M., Pfeffer, K.*, Tragverhalten zweiachsiger Hohlkörper-decken. *Beton- und Stahlbetonbau* 96, 2001, Heft 9, S.573-578.